npj | Quantum Materials

www.nature.com/npjquantmats

ARTICLE OPEN

Electronic band tuning under pressure in $MoTe_2$ topological semimetal

Sachith Dissanayake[1,6], Chunruo Duan[2], Junjie Yang[3], Jun Liu[4], Masaaki Matsuda[1], Changming Yue[5], John A. Schneeloch[2], Jeffrey C. Y. Teo[2] and Despina Louca[2]

Topological superconductors (TSC) can host exotic quasiparticles such as Majorana fermions, poised as the fundamental qubits for quantum computers. TSC's are predicted to form a superconducting gap in the bulk, and gapless surface/edges states which can lead to the emergence of Majorana zero energy modes. A candidate TSC is the layered dichalcogenide $MoTe_2$, a type-II Weyl (semi) metal in the non-centrosymmetric orthorhombic (T_d) phase. It becomes superconducting upon cooling below 0.25 K, while under pressure, superconductivity extends well beyond the structural boundary between the orthorhombic and monoclinic (1T′) phases. Here, we show that under pressure, coupled with the electronic band transition across the T_d to 1T′ phase boundary, evidence for a new phase, we call T_d* is observed and appears as the volume fraction of the T_d phase decreases in the coexistence region. T_d* is most likely centrosymmetric. In the region of space where T_d* appears, Weyl nodes are destroyed. T_d* disappears upon entering the monoclinic phase as a function of temperature or on approaching the suppression of the orthorhombic phase under pressure above 1 GPa. Our calculations in the orthorhombic phase under pressure show significant band tilting around the Weyl nodes that most likely changes the spin-orbital texture of the electron and hole pockets near the Fermi surface under pressure that may be linked to the observed suppression of magnetoresistance with pressure.

npj Quantum Materials (2019)4:45 ; https://doi.org/10.1038/s41535-019-0187-7

INTRODUCTION

A Weyl (semi)metal is a new topological state of matter that hosts the condensed matter equivalent of relativistic Weyl fermions. Weyl fermions exist as low-energy electronic excitations at Weyl nodes in three-dimensional momentum space, producing exotic physical properties such as unique surface Fermi arcs and negative magnetoresistance.[1–4] The topological Weyl state can be realized by breaking either time-reversal or lattice inversion symmetry. A candidate topological Weyl semimetal is the quasi two-dimensional transition metal dichalcogenide $MoTe_2$.[5–8] The transition to the non-trivial topologically protected crystal state occurs upon cooling from the high temperature 1T′ monoclinic phase to the low temperature orthorhombic T_d phase. The transition is driven by *c*-axis layer stacking order around 250 K.[9–13] Upon cooling to the non-centrosymmetric T_d phase, Weyl quasiparticles are expected at characteristic electron and hole band crossings in momentum space.

$MoTe_2$ is a candidate TSC in the orthorhombic phase at ambient pressure.[14] In the superconducting state, Fermi arcs are proposed to still exist even though the Weyl nodes are completely gapped out by the superconducting gap, and the onset of superconductivity can generate a quantum anomaly analogous to the parity anomaly in quantum electrodynamics.[15,16] The application of pressure enhances the superconducting transition temperature from 0.25 to about 8 K[14] and extends the superconducting phase over a wide pressure range. Recent studies showed that while in the superconducting state, a phase transition occurs from the orthorhombic T_d to the monoclinic 1T′ phase under pressure[17] with a large hysteresis region and coexistence of the two phases. A high-pressure muon-spin rotation study of superconductivity in $MoTe_2$ suggested that a topologically non-trivial s^{+-} state likely exists in $MoTe_2$ at pressures up to 1.9 GPa.[18] Key components to a TSC state are the crystal structure and band topology under pressure. Existing reports stop short of exploring the symmetry in the superconducting phase under pressure and no calculations exist on the electronic band structure. Using single crystal neutron diffraction, the pressure–temperature phase diagram is mapped out, and combined with band structure calculations, we elucidate the effects of pressure on the electronic band structure topology. The results provide evidence for a topological state that persists under pressure, consistent with the muon work of ref. [18].

$MoTe_2$ can crystallize into several different structures including the hexagonal 2H, the monoclinic 1T′ and the low temperature orthorhombic T_d phases.[9–11] The hexagonal 2H phase (with space group $P6_3/mmc$), a semiconductor with an indirect band gap of 0.88 eV, is stable below 900 °C.[19,20] The monoclinic 1T′ phase is stable above 900 °C but can be stabilized to room temperature by quenching.[9,10,20] In the 1T′ phase, Mo is surrounded by Te in an octahedral environment with Mo shifted off-center. Mo atoms form zigzag chains running along the *b*-axis that distort the Te sheets resulting in a tilted *c*-axis with angle $\beta \sim 93°$ (Fig. 1a).[9] Upon cooling from the 1T′ and not from the 2H phase, a first order structural transition occurs into the orthorhombic T_d phase (Fig. 1b). This transition comes about as a result of layer stacking order along the *c*-axis in the T_d phase.[13]

[1]Neutron Scattering Division, Oak Ridge National Laboratory, Oak Ridge, TN 37831, USA; [2]Department of Physics, University of Virginia, Charlottesville, VA 22904, USA; [3]Department of Physics, Central Michigan University, Mount Pleasant, MI 48859, USA; [4]Ames Laboratory of U.S. Department of Energy, Ames, Iowa 50011, USA; [5]Institute of Physics, Chinese Academy of Sciences, Beijing, China and [6]Present address: Department of Physics, Duke University, Durham, NC 27708, USA
Correspondence: Despina Louca (louca@virginia.edu)

Received: 28 March 2019 Accepted: 30 July 2019
Published online: 16 August 2019

Published in partnership with Nanjing University

npj nature partner journals

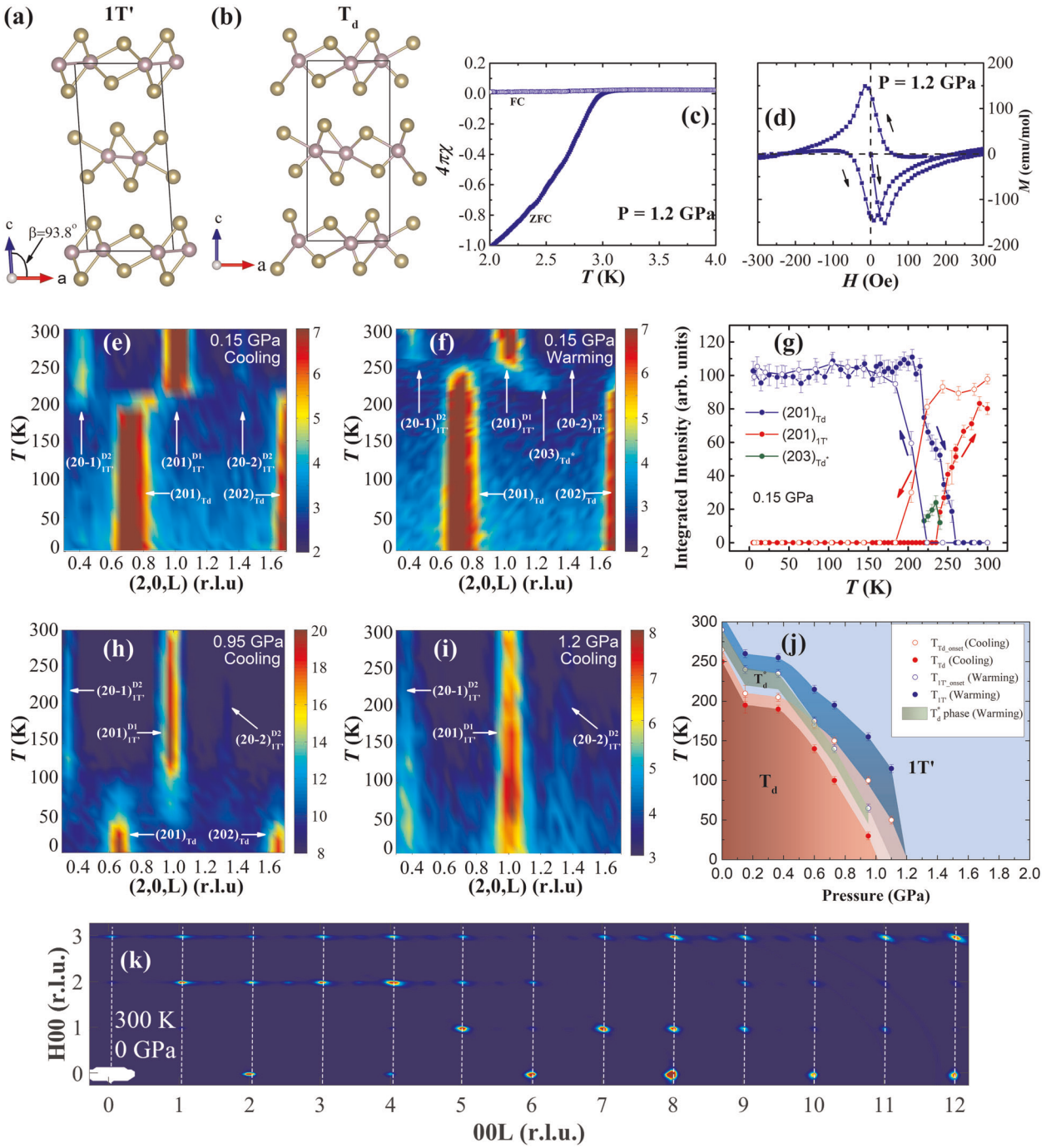

Fig. 1 Physical properties. **a** Crystal structure of $MoTe_2$ in the 1T′ phase projected on the *ab*-plane, with the zigzag chains marked running along the *a*-axis. **b** Unit cell of the T_d structure projected on the *ac* plane. **c** Temperature-dependent superconducting (SC) shielding [zero-field-cooled (ZFC)] and Meissner (FC) fraction data for $MoTe_2$ in $H = 20$ Oe at 1.2 GPa. **d** Magnetic hysteresis loop for $MoTe_2$ at 2 K at 1.2 GPa. Arrows indicate sweeping direction. **e**, **f** Contour map of the neutron scattering intensity obtained by scanning across the (2 0 *l*) Bragg peak along the [0 0 1] direction at 0.15 GPa on cooling (**e**) and warming (**f**). The peak labels denoted with D1 (main domain) and D2 (second domain) are used to distinguish the peaks coming from two different domains, and subscripts 1T′ and T_d are used to distinguish the peaks in the different phases. **g** Temperature dependence of the *q* integrated neutron scattering intensity for $(201)^{D1}_{1T'}$ peak (red squares), $(201)_{T_d}$ peak (blue circles), and $(201)_{T_d*}$ (green circles). Arrows indicate sweeping directions. **h**, **i** Contour map of the neutron scattering intensity obtained by scanning across the (2 0 *l*) Bragg peak along the [0 0 1] direction at 0.95 GPa on cooling (**h**) and at 1.2 GPa on cooling (**i**). **j** The phase diagram under pressure. The region between the two phases shows coexistence of both phases plus the T_d* phase. Inversion symmetry is broken only in the T_d phase while both T_d* and 1T′ are centrosymmetric. **k** A two-dimensional scan in the h0l plane outside the pressure cell with half-integer peaks from the T_d* phase appearing along L. The dashed white lines mark the integer peaks along L that correspond to both the T_d and T_d* phases while the half-integer peaks belong to the T_d* phase only

Table 1. Crystal unit cell parameters

	Mo1	Mo2	Mo3	Mo4	Te1	Te2	Te3	Te4	Te5	Te6	Te7	Te8
x	0.893	0.746	0.321	0.321	0.502	0.355	0.578	0.578	0.147	0.000	0.932	0.932
z	0.251	0.751	0.497	0.997	0.300	0.800	0.071	0.571	0.173	0.673	0.444	0.944

Atom coordinates of the proposed T_d* structure. The space group is P21/m, with a = 6.33 Å, b = 3.47 Å, c = 27.66 Å, and with the y-coordinates set at 0 for all atoms

RESULTS

Shown in Fig. 1c, d are the plots of the bulk magnetic susceptibility, χ(T), and magnetization, *M*, under pressure as a function of temperature and magnetic field, respectively. Our crystal becomes diamagnetic below 3.0 K at 1.2 GPa, marking the onset of superconductivity. Bulk superconductivity is evident in the full shielding diamagnetic signal at 2.0 K. Note that χ(T) was measured along the *ab*-plane in which the demagnetizing factor is negligible. The crystal exhibits a large shielding fraction, ~100% (zero-field-cooled (ZFC) magnetization), at 2 K and 1.2 GPa. Magnetic hysteresis loops were also measured at 2.0 K and 1.2 GPa as shown in Fig. 1d indicating that $MoTe_2$ exhibits a typical type-II superconducting behavior.

The 1T′ to T_d phase transition under pressure was explored by single crystal neutron diffraction performed in the *20L* scattering plane, focusing on structural signatures most affected by variations in the angle β between the *a*- and *c*-axes. The crystal was aligned using the lattice constants and β of the 1T′ symmetry ($a = 6.3263$ Å, $b = 3.469$ Å, $c = 13.7789$ Å, $\alpha = 90°$, $\beta = 93.75°$, $\gamma = 90°$). A typical contour map of the scattering intensity as a function of temperature at constant pressure is shown in Fig. 1e at 0.15 GPa. At 300 K in the 1T′ phase, a very strong Bragg peak at $(hkl) = (2\,0\,1)$ is observed along with two weak secondary peaks, at (0.4 0 1) and (1.4 0 1). The Bragg peaks are from the two possible domains in the monoclinic symmetry and are marked with superscripts D1 and D2 indicating domain one and two, respectively. One domain (D1) is overwhelmingly more intense than the other and the crystal was aligned using the primary domain. At 0.15 GPa, the 1T′ to T_d phase transition is clearly observed upon cooling, with a discontinuous volume change and the transition temperature shifting to a lower value compared to the ambient pressure value (~240 K). At the transition from 1T′ to T_d at 220 K, the 1T′ $(201)^{D2}_{1T'}$, $(201)^{D1}_{1T'}$ and $(202)^{D2}_{1T}$ peaks disappear and the T_d peaks, $(201)_{T_d}$ and $(202)_{T_d}$, appear as shown in Fig. 1e. The $(201)_{T_d}$ and $(202)_{T_d}$ peaks appear at different/positions corresponding to the change of β from 93.75° (1T′) to 90° (T_d). There is only a single domain and one set of peaks in the T_d phase. Alignment of the single crystal remained the same as at 300 K during cooling. On warming, a similar set of Bragg peaks is observed and shown in the contour map of Fig. 1f as on cooling but with an additional Bragg peak that arises from the new T_d* phase. While only one peak at $(203)_{T_d*}$ is present in this narrow range of the 20 L scan inside the pressure cell, other T_d* peaks have been observed along L. This is shown in the 2D plot of the H0L scattering plane from a single crystal measurement at 300 K outside the pressure cell (Fig. 1k). T_d* peaks appear at half-integer L-points and are prominent along 20 L and 30 L. No T_d* peaks are visible on cooling which is consistent with earlier single crystal neutron diffraction measurements (see ref. [21]). A thermal hysteresis is evident with the transition temperature shifting to 250 K on warming, which is higher than that on cooling, consistent with the thermal hysteresis observed at ambient pressure and in transport measurements.[21] The temperature dependence of the integrated intensities for $(201)^{D1}_{1T'}$, $(201)_{T_d}$ and $(201)_{T_d*}$ Bragg peaks are shown in Fig. 1g, where coexistence of the two phases appears in the hysteresis region while the T_d* phase only exists in the coexistence region. The structure parameters for the T_d* phase obtained from the data outside the pressure cell are provided in Table 1. The T_d* phase grows at the expense of the T_d phase. At no point in pressure or temperature do we observed the T_d* phase becoming the only phase, indicating that T_d and T_d* coexist. T_d* disappears upon further warming into the 1T′ phase. At 0.15 GPa and 230 K data, all three phases coexist (Fig. 1g).

As the pressure increases to higher values, a precipitous decrease of the 1T′ to T_d transition temperature occurs, eventually leading to the disappearance of the T_d Bragg peaks by about 1.2 GPa. The intensity plot of Fig. 1h at 0.95 GPa clearly shows the phase transition temperature going down until its complete disappearance by 1.2 GPa as shown in Fig. 1i. At 1.2 GPa, only 1T′ Bragg peaks are observed in the temperature range from 5 to 300 K, regardless of the thermal cycling. Note that the two-domain feature of the 1T′ phase is observed at all pressure points. The single crystal results were additionally confirmed by neutron powder diffraction measurements under pressure that reached down to 1.5 K. The phase diagram under pressure is shown in Fig. 1j. Shown on the diagram are three distinct regions: the high temperature monoclinic region, the low temperature orthorhombic region and the coexistence region between the two that is also host to the new T_d* phase. On warming, the T_d* phase appears up to about 1 GPa; unit cell doubling occurs in the coexistence region of the two phases that disappears upon applying pressure greater than 1 GPa. This is shaded in green on the phase diagram. Above 1 GPa, a broad transition from the T_d to 1T′ with apparent phase coexistence is observed. Coupled with the transition to the monoclinic phase under pressure is suppression of the magnetoresistance[22] which may be linked to the disappearance of the Weyl nodes.

Shown in Fig. 2 is a comparison of the Fermi surface projected on the k_x–k_y momentum plane in the orthorhombic T_d phase, calculated at two pressure points, 0 GPa (upper panels) and 0.15 GPa (lower panels). At 0 GPa, the two Weyl points indicated by dots in the k_x–k_y plane at $k_z = 0$ and at $E - E_F = 23$ and 52.5 meV appear at the intersection of electron and hole pockets as indicated in both figures and also in the band structure diagram on the right where the crossing points in the dispersion are marked by the letters A and B. These Weyl nodes are the same as those reported in ref. [21]. Increasing the pressure to 0.15 GPa changes the *c*-axis lattice constant by about 0.5% (with negligible change in the *a*-axis lattice constant). At 0.15 GPa, new nodes appear at $E - E_F = 18$ and 58 meV above the Fermi level, on the same band as the nodes at $E - E_F = 23$ and 52.5 meV at 0 GPa, but at $k_z \neq 0$. At 0.15 GPa, the superconducting transition temperature increases as reported in ref. [14] while magnetoresistance goes down.[22] The same nodes could not be traced in the band dispersions from calculations performed at higher pressures. At pressure values exceeding 1.2 GPa, the 1T′ symmetry is centrosymmetric and no Weyl nodes are expected. Ambient pressure calculations confirmed that the 1T′ with the $P2_1/m$ space group remains topologically trivial.[13] Thus, with warming from the T_d to T_d* and then to the 1T′ phase, the type-II Weyl nodes are destroyed.[13]

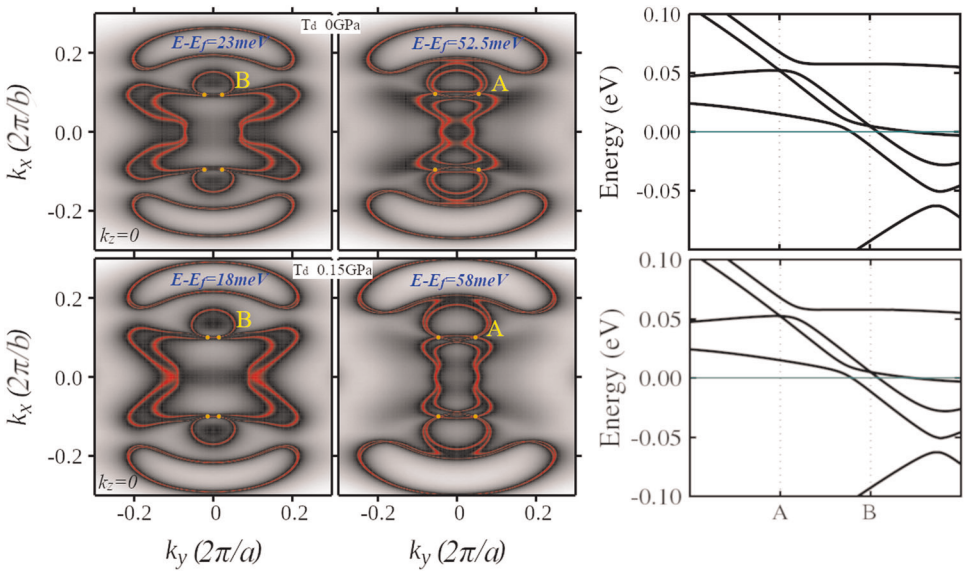

Fig. 2 Electronic Structure: The top panels are calculations performed in the T_d phase at 0 GPa. The lower panels are calculations performed at 0.15 GPa in the T_d phase. The Fermi surface cuts shown on the left panels reveal the Weyl nodes at the intersections of electron and hole pockets. These are marked by A and B. The right panels are band structure plots showing the bands crossing at A and B

DISCUSSION

Analysis of the Berry curvature of the new nodes that appear in the T_d phase from the band structure calculations performed at 0.15 GPa shown in Fig. 2 indicates that indeed these new crossings are not trivial. This is demonstrated in Fig. 3 which is a comparison of the energy isosurfaces and dispersion relations of the Weyl nodes at $P = 0$ and at 0.15 GPa in the T_d phase. The Fermi surface morphology changes under pressure as seen from Fig. 2 while the Weyl nodes, observed closed to the Γ point and indicated by A and B in the plots of Fig. 2, change energy. Calculations of the energy isosurface at the nodes based on k·p perturbation theory suggest that the Weyl nodes are still type-II as shown in the line plots of Fig. 3 for the two Weyl nodes in the T_d phase at 0 and 0.15 GPa at the corresponding k-points, but become significantly tilted under pressure, especially for the second Weyl node at 18 meV. The values of E, k_x, k_y, and k_z for the two Weyl points are provided in Table 2. These results suggest that with the enhancement of superconductivity, the phase remains topologically non-trivial. Moreover, changes in the Berry curvature may be linked to the decrease in magnetoresistance under pressure.[22]

Last, we comment on the prospect of topological superconductivity in the material. While superconductivity is observed in $MoTe_2$ in the T_d and 1T′ phases under a range of pressures, topological superconductivity is not guaranteed unless the following two conditions are satisfied: In (i), the Weyl fermions have to either be responsible or take part in the superconducting pairing. And in (ii), assuming the pairing order is s-wave and does not break time-reversal symmetry spontaneously, the sign of the pairing order parameter must be non-uniform. Reference [23] shows that the integral topological index N, which counts the (net chiral) number of surface Majorana cones, is related to the combination of signs $\sum_j c_j \mathrm{sgn}(\Delta_j)/2$, where c_j is the chirality of the jth Weyl fermion and $\mathrm{sgn}(\Delta_j)$ is the sign of its pairing order parameter in the Bogoliubov-de Gennes Hamiltonian. Trivial Fermi surfaces that have trivial Chern numbers do not affect the topology of the superconducting state assuming the pairing order is BCS s-wave. First, the type-II nature of the Weyl cones in $MoTe_2$ provides a huge hyperbolic Fermi surface and density of state at the Fermi level, both of which favor condition (i). Second, thanks to the small crystal symmetry group of the material, the Weyl points are not related to each other, other than by time-reversal. In contrast with Weyl (semi)metals with large crystal symmetry group, such as the TaAs family, the pairing order parameters of different Weyl fermions are related by lattice rotation and/or mirror symmetries assuming they are not spontaneously broken. In order of these parameters to take non-uniform value, a strong symmetry breaking field or deformation is needed. On the other hand, for the current small symmetry present in $MoTe_2$ material class, there is no such requirement. Consequently, the pairing response to deformations, such as thermal and crystal structural changes, can be different between unrelated Weyl fermions, and may lead to non-uniform pairing signs through phase transitions driven by external tuning parameters. For instance, in Table 2 we show that the tilting behavior of the Weyl points along the principal axes can change as a function of pressure. While conditions (i) and (ii) as well as the protected surface Majorana fermions are yet to be verified, $MoTe_2$ can be a promising material for further investigation due to its Weyl electronic structure's strong dependence on thermal and structural parameters.

METHODS

Meaurements

$MoTe_2$ single crystals were grown by self-flux method. The details of single crystal growth have been described elsewhere.[16] The typical size of the obtained single crystals is about $4 \times 2 \times 1\ mm^3$. Single crystal neutron diffraction under high pressure is combined with electronic band structure calculations to investigate the superconducting transition. Our $MoTe_2$ single crystal exhibits a superconducting transition near 3 K at 1.2 GPa from bulk magnetic susceptibility measurements under pressure. The bulk magnetic susceptibility was measured at high pressure using a vibrating sample magnetometer (VSM) to demonstrate the superconducting transition in our $MoTe_2$ single crystals. The applied pressure was calibrated by measuring pressure cell compression and the pressure dependence of the superconducting transition temperature of a tiny lead piece. High-pressure neutron diffraction experiments were performed on single crystals at HB-1A triple axis spectrometer and using powders at HB-2A powder diffractometer at the High Flux Isotope Reactor (HFIR) of Oak Ridge National Laboratory (ORNL). Self-clamped piston cylinder cells made with CuBe was used as pressure cells for both bulk magnetic susceptibility measurements and neutron diffraction experiments. Daphne 7373 oil was chosen as the pressure transmitting medium. Single crystal neutron

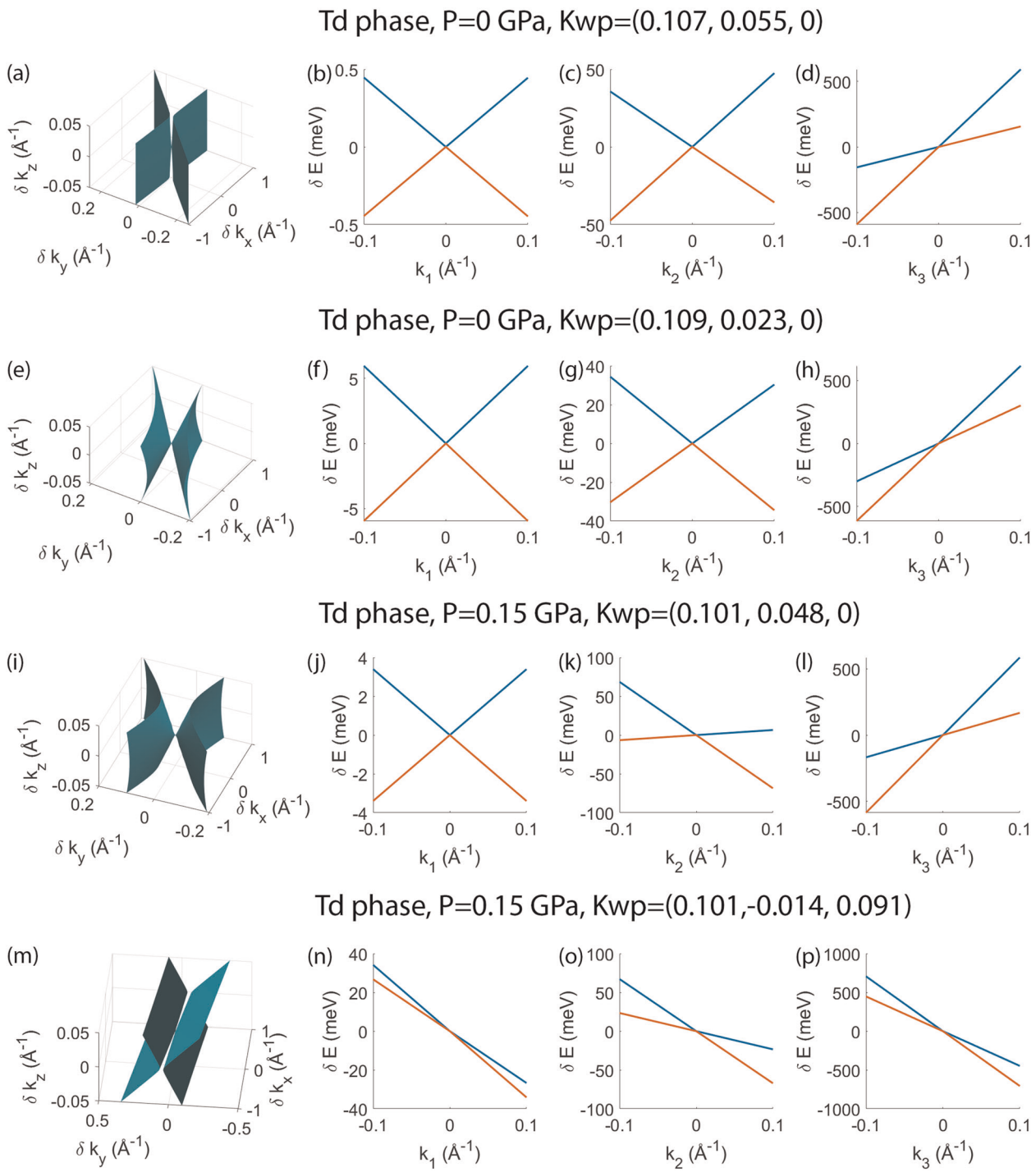

Fig. 3 k.p calculations: Energy isosurfaces and dispersion relations of the Weyl nodes in T_d phase are shown in the figure: **a**–**h** T_d phase at 0.0 GPa, **i**–**p** T_d phase at 0.15 GPa. The isosurfaces have the same energy as the corresponding Weyl nodes, and the dispersion plots are along the three principle axes of the matrix M. The existence of such energy isosurfaces and dispersion relations indicates that the Weyl nodes are type-II

diffraction were performed at HB1 triple axis spectrometer with a fixed incident neutron energy of 13.5 meV. The lattice constant measurements of NaCl were used to calibrate the pressure. The single crystal neutron diffraction data shown in Fig. 1k were collected at the CORELLI spectrometer at ORNL.

Calculations

The theoretical DFT calculation was implemented in the Vienna Ab initio Simulation Package (VASP) for the pressurized T_d and 1T′ phases of $MoTe_2$. VASP is a plane-wave based projector augmented pseudopotential local density functional method. Its exchange-correlation functional takes the generalized gradient approximation parameterized by Perdew-Burke-Ernzerhof. We turned on the spin–orbit coupling, used the default energy cutoff for the calculation and chose a K-grid of 13*7*3. An NBANDS of 160 is used to allow enough bands for Wannier90 to fit a minimum basis tight binding Hamiltonian involving Mo's 4d and Te's 5p orbits with necessary symmetrization. We used Wannier_tools for ab initio data processing, including nodal searching, Chirality calculation, and Fermi surface contour

Table 2. Electronic structure parameters

	T_d			
P (GPa)	0		0.15	
E (eV)	0.0537	0.0053	0.058	0.0187
k_x	0.1071	0.1091	0.1007	0.101
k_y	0.0548	0.0227	0.0478	−0.0135
k_z	0	0	0	0.0907
v_x^+ (eV · Å)	0.0045	0.0595	0.0340	−0.2674
v_y^+ (eV · Å)	0.4754	0.3035	0.0655	−0.2341
v_z^+ (eV · Å)	5.9155	6.1564	5.8641	−4.4762
v_x^- (eV · Å)	−0.0045	−0.0596	−0.0340	−0.3415
v_y^- (eV · Å)	−0.3575	−0.3443	−0.6858	−0.6715
v_z^- (eV · Å)	1.5610	3.0122	1.6813	−7.0697
ψ (°)	74.36	65.11	70.94	−83.94
θ (°)	−90.00	−90.00	−90.00	−4.03
ϕ (°)	−79.87	−71.38	−80.21	−84.70

List of the Weyl node energy, k-space coordinates, group velocity components of the two bands crossing at all the Weyl nodes along the principle axes of the M matrix, as well as the Tait-Bryan Euler angles (rotation order: ZYX) of the principle axes. The k-space coordinates of the nodes are given below with reciprocal vectors taken as the unit vectors. Since the dispersion should have weak dependence on k_z, two related Weyl points can have somewhat different k_z values, but the FS surface topologies are quite similar as seen from the figure

plot. For the T_d phases, the lattice constant for 0 GPa is $a = 6.2977$ Å, $b = 3.474$ Å, $c = 13.8286$ Å, the lattice constant for 0.15 GPa is $a = 6.3213$ Å, $b = 3.461$ Å, $c = 13.7499$ Å. For the 1T′ phases, the lattice constant for 0 GPa is $a = 6.33$ Å, $b = 3.469$ Å, $c = 13.86$ Å with $\beta = 93°$, the lattice constant for 0.15 GPa is $a = 6.3263$ Å, $b = 3.467$ Å, $c = 13.7789$ Å with $\beta = 93.75°$, the lattice constant for 1.2 GPa is $a = 6.2954$ Å, $b = 3.4601$ Å, $c = 13.4766$ Å with $\beta = 94.183°$, the lattice constant for 1.8 GPa is $a = 6.294$ Å, $b = 3.456$ Å, $c = 13.381$ Å with $\beta = 94.183°$. The coordinates of Mo and Te atoms at 0 GPa are obtained from the refinement of the neutron scattering results while for systems under pressure they are simply rescaled to the new lattice constant obtained under pressure.

In the k.p perturbation theory, the Hamiltonian is expanded up to the first order term near each of the Weyl nodes. In the basis of the two bands that crosses at the Weyl node, the Hamiltonian can be written as a 2 by 2 matrix. A 2 by 2 Hermitian matrix has four independent variables, so for a 3D case the p part of the Hamiltonian will have totally 12 independent variables. With the help of Pauli matrices the k.p Hamiltonian can be expressed in the following form:

$$H(\vec{w} + \delta\vec{k}) = [\varepsilon(\vec{w}) + \delta\vec{k} \cdot \vec{v}_0]\sigma^0 + \delta\vec{k} \cdot R \cdot \vec{\sigma}^T$$

Here $\vec{w}$ is the reciprocal vector of a Weyl node, $\varepsilon(\vec{w})$ is the energy at that node, σ^0 is the 2×2 identity matrix, $\vec{\sigma}^T = (\sigma^1, \sigma^2, \sigma^3)^T$ is the vector formed by the three Pauli matrices, $\vec{v}_0$ and R are real 1 by 3 vector and 3 by 3 matrix that contain the 12 independent varibles. The energy dispersion near the Weyl node can then be solved analytically:

$$E^{\pm}(\vec{w} + \delta\vec{k}) = \varepsilon(\vec{w}) + \delta\vec{k} \cdot \vec{v}_0 \pm \sqrt{\delta\vec{k} \cdot M \cdot \delta\vec{k}^T}$$

Where $M = 3R \cdot R^T$ is a real symmetric matrix. The group velocity along any given direction on each of the two crossing bands at each Weyl nodes can be calculated using the DFT method described above. The vector $\vec{v}_0$ and the matrix M can then be determined from these velocity data.

DATA AVAILABILITY

The neutron data collected for this project can be made available to interested researchers upon request. Similarly for the data collected for bulk characterization.

ACKNOWLEDGEMENTS

The work at Central Michigan University was supported by the FRCE program under Grant No. 48846. The work at the University of Virginia is supported by the Department of Energy, Grant number DE-FG02-01ER45927 and by the National Science Foundation under Grant No. DMR-1653535. The work at the High Flux Isotope Reactor at Oak Ridge National laboratory is sponsored by the Scientific User Facilities Division, Office of Basic Energy Sciences, U.S. Department of Energy.

AUTHOR CONTRIBUTIONS

S.D. led the neutron experiment under pressure and contributed to the writing of the paper. M.M. contributed to the neutron experiment. J.Y. and J.A.S. contributed samples for this experiment. J.Y. led the characterization of superconductivity under pressure, and contributed to the writing of the paper. J.L. and C.Y. carried out the density functional theory calculations. C.D. and J.C.Y. Teo carried out the k.p calculations. C.D. and J.A.S. contributed to the identification of the T_d* phase. D.L. wrote the paper and led the project.

ADDITIONAL INFORMATION

Competing interests: The authors declare no competing interests.

Publisher's note: Springer Nature remains neutral with regard to jurisdictional claims in published maps and institutional affiliations.

REFERENCES

1. Yan, B. & Felser, C. Topological materials: Weyl semimetals. *Annu. Rev. Condens. Matter Phys.* **8**, 337–354 (2017).
2. Soluyanov, A. A. et al. Type-II Weyl semimetals. *Nature* **527**, 495–498 (2015).
3. Weng, H., Fang, C., Fang, Z., Bernevig, B. A. & Dai, X. Weyl semimetal phase in noncentrosymmetric transition-metal monophosphides. *Phys. Rev. X* **5**, 011029 (2015).
4. Xu, S.-Y. et al. Discovery of a Weyl fermion semimetal and topological Fermi arcs. *Science* **349**, 613–617 (2015).
5. Sun, Y., Wu, S.-C., Ali, M. N., Felser, C. & Yan, B. Prediction of Weyl semimetal in orthorhombic $MoTe_2$. *Phys. Rev. B* **92**, 161107 (2015).
6. Deng, K. et al. Experimental observation of topological Fermi arcs in type-II Weyl semimetal $MoTe_2$. *Nat. Phys.* **12**, 1105–1110 (2016).
7. Huang, L. et al. Spectroscopic evidence for a type II Weyl semimetallic state in $MoTe_2$. *Nat. Mater.* **15**, 1155–1160 (2016).
8. Tamai, A. et al. Fermi arcs and their topological character in the candidate type-II Weyl semimetal $MoTe_2$. *Phys. Rev. X* **6**, 031021 (2016).
9. Clarke, R., Marseglia, E. & Hughes, H. P. A low-temperature structural phase-transition in β-$MoTe_2$. *Philos. Mag. B* **38**, 121–126 (1978).
10. Brown, B. E. The crystal structures of WTe_2 and high-temperature $MoTe_2$. *Acta Cryst.* **20**, 268–274 (1966).
11. Puotinen, D. & Newnham, R. E. The crystal structure of $MoTe_2$. *Acta Cryst.* **14**, 691–692 (1961).
12. Hughes, H. P. & Friend, R. H. Electrical resistivity anomaly in β-$MoTe_2$. *J. Phys. C: Solid State Phys.* **11**, L103–L105 (1978).
13. Schneeloch, J. A. et al. Emergence of topologically protected states in the $MoTe_2$ Weyl semimetal with layer stacking order. *Phys. Rev. B.* **99**, 161105 (2019).
14. Qi, Y. et al. Superconductivity in Weyl semimetal candidate $MoTe_2$. *Nat. Commun.* **7**, 11038 (2016).
15. Alidoust, M., Halterman, K. & Zyuzin, A. A. Superconductivity in type-II Weyl semimetals. *Phys. Rev. B* **95**, 155124 (2017).
16. Wang, R., Hao, L., Wang, B. & Ting, C. S. Quantum anomalies in superconducting Weyl metals. *Phys. Rev. B* **93**, 184511 (2016).
17. Heikes, C. et al. Mechanical control of crystal symmetry and superconductivity in Weyl semimetal $MoTe_2$. *Phys. Rev. Mater.* **2**, 074202 (2018).
18. Guguchia, Z. et al. Signatures of the topological s^{+-} superconducting order parameter in the type-II Weyl semimetal T_d-$MoTe_2$. *Nat. Commun.* **8**, 1082 (2017).
19. Keum, D. H. et al. Bandgap opening in few-layered monoclinic $MoTe_2$. *Nat. Phys.* **11**, 482–486 (2015).
20. Reshak, A. H. & Auluck, S. Band structure and optical response of 2H-MoX_2 compounds (X = S, Se, and Te). *Phys. Rev. B* **71**, 155114 (2005).
21. Yang, J. et al. Elastic and electronic tuning of magnetoresistance in $MoTe_2$. *Sci. Adv.* **3**, eaao4949 (2017).
22. Lee, S. et al. Origin of extremely large magnetoresitance in the candidate type-II Weyl semimetal $MoTe_{2-x}$. *Sci. Rep.* **8**, 13937 (2018).
23. Qi, X.-L., Hughes, T. L., Raghu, S. & Zhang, S.-C. Time-reversal-invariant topological superconductors and superfluids in two and three dimensions. *Phys. Rev. Lett.* **102**, 187001 (2009).